



Zonal variability of methane trends derived from satellite data

Jonas Hachmeister¹, Oliver Schneising¹, Michael Buchwitz¹, John P. Burrows¹, Justus Notholt¹, and Matthias Buschmann¹

¹Institute of Environmental Physics (IUP), University of Bremen FB1, Bremen, Germany

Correspondence: J. Hachmeister (jonas_h@iup.physik.uni-bremen.de)

Abstract. The Tropospheric Monitoring Instrument (TROPOMI) on-board the satellite Sentinel-5 Precursor (S5P) is part of the latest generation of trace gas monitoring satellites and provides a new level of spatio-temporal information with daily global coverage, which enable the calculation of daily globally averaged CH₄ concentrations. To investigate changes of atmospheric methane, the background CH₄ level (i.e. the CH₄ concentration without seasonal and short-term variations) has to be determined. CH₄ growth rates vary in a complex manner and high-latitude zonal averages may have gaps in the time series, thus simple fitting methods don't produce reliable results. In this manuscript we present an approach based on fitting an ensemble of Dynamic Linear Models (DLMs) to TROPOMI data, from which the best model is chosen with the help of cross-validation to prevent overfitting. We present results of global annual methane increases (AMIs) for the first 4.5 years of S5P/TROPOMI data which show good agreement with AMIs from other sources. Additionally, we investigated what information can be derived from zonal bands. Due to the fast meridional mixing within hemispheres we use zonal growth rates instead of AMIs, since they provide a daily temporal resolution. Clear differences can be observed between Northern and Southern Hemisphere growth rates, especially during 2019 and 2022. The growth rates show similar patterns within the hemispheres and show no short-term variations during the years, indicating that air masses within a hemisphere are well-mixed during a year. Additionally, the growth rates derived from S5P/TROPOMI data are largely consistent with growth rates derived from CAMS global inversion-optimized (CAMS/INV) data. In 2019 a reduction in growth rates can be observed for the Southern Hemisphere, while growth rates in the Northern Hemisphere stay stable or increase. During 2020 a strong increase in Southern Hemisphere growth rates can be observed, which is in accordance with recently reported increases in Southern Hemisphere wetland emissions. In 2022 the reduction of the global AMI can be attributed to decreased growth rates in the Northern Hemisphere, while growth rates in the Southern Hemisphere remain high. Investigations of fluxes from CAMS/INV data support these observations and suggest that the Northern Hemisphere decrease is mainly due to the decrease in anthropogenic fluxes while in the Southern Hemisphere wetland fluxes continued to rise.

1 Introduction

Methane (CH₄) is one of the most important drivers of climate change with an effective radiative forcing of 1.19 Wm⁻² (Arias et al., 2021) and an atmospheric lifetime of 9.1 years (Szopa et al., 2021). The short lifespan of CH₄ compared to other greenhouse gases and the large fraction of anthropogenic emissions, makes CH₄ emission reduction a straight forward way to tackle climate change in the short- to midterm. A close monitoring of atmospheric CH₄ concentrations is therefore vital, both



for scientists and policymakers. The globally averaged surface concentration of CH₄ has increased by 156% between 1750 and 2019 reaching 1866 ± 3.3 ppb in 2019 (Gulev et al., 2021) and 1919.97 ppb in February 2023 (Lan et al., 2023). While the concentrations have risen in total, the trend, i.e. the rate of change in the background level without seasonal or short-term variations, has evolved non-linearly. An increase in global methane concentrations can be observed between the 1980s-2000 and from 2007 until the present, with a plateau between 2000-2007 which is referred to as “stabilization“. Whether to define the stabilization period or the period of renewed growth (2007-present) as anomalous has been the subject of debate. There have been a variety of explanations for the observed behavior in the literature (Turner et al., 2019). Recent publications suggest that the period of renewed growth can be attributed to the rise in microbial emissions (Lan et al., 2021; Basu et al., 2022) and that tropical methane emissions explain a majority of recent changes in the atmospheric methane growth rate (Feng et al., 2022). In 2020 and 2021 record methane increases were observed by the Global Monitoring Laboratory of the ‘National Oceanic and Atmospheric Administration (NOAA-GML) (Lan et al., 2023) and the Copernicus Climate Change Service (C3S) (C3S, 2023a). The reasons for these increases are still debated, with studies attributing them to increases in wetland emissions and changes in the atmospheric methane sink to varying degrees. The main sink of methane is through reaction with the hydroxyl radical (OH) in the troposphere, which itself is affected by various other atmospheric constituents. Recent studies suggest that the steep decline of nitrogen dioxide (NO₂) (Cooper et al., 2022), carbon monoxide (CO) and non-methane volatile organic compound emissions as a result of the measures introduced to control and limit the spread of the COVID-19 pandemic, lowered the levels of OH, and thus led to part of the increase in CH₄ concentrations in 2020 and 2021 (Stevenson et al., 2022; Laughner et al., 2021; Peng et al., 2022; Qu et al., 2022; Feng et al., 2023). Additionally, enhanced wetland emissions, especially from tropical wetlands, contributed to the record increases in 2020/21 (Peng et al., 2022; Feng et al., 2023, 2022; Qu et al., 2022). A potential uncertainty in studies using ground-based data originates in the high latitude regions, where measurements are sparse and satellites can help with identifying methane emissions. The Arctic contains large amounts of soil organic carbon (SOC) which is stored in the permafrost regions (ca. 1300 Pg) of which roughly 800 Pg is perennially frozen (Hugelius et al., 2014). The comparatively high temperature increase in the Arctic, compared to the rest of the world, also called “Arctic amplification“ (Serreze and Barry, 2011; Wendisch et al., 2017) may lead to increased permafrost degradation and rapid SOC loss (Plaza et al., 2019) by the release of carbon dioxide (CO₂) and/or methane. Latitudinally resolved growth rates are especially interesting in this regard and provided the initial motivation for this study. In this paper we present methane growth rates and annual methane increases (AMIs) derived from Sentinel-5P/TROPOMI data using a Dynamic Linear Model (DLM) approach. In the second section we present the data used. Next, we describe our method for calculating the growth rates, which is divided into four parts: (i) we discuss the preparation of the data; (ii) we provide a brief introduction into DLMs; (iii) we discuss our ensemble approach which utilizes cross validation to find the optimal DLM configuration for a given time series; (iv) we provide a method to calculate a bias related to the satellite sampling. In the fourth section we present global annual methane increases (AMIs) for the first 4.5 years of S5P/TROPOMI data and compare these to AMIs from other sources. In the fifth section we investigate zonal growth rates derived from 20° latitudinal bands to provide spatial information to the global AMIs. Additionally, we compare the growth rates to growth rates derived from CAMS global inversion-optimized methane data (CAMS/INV). In the



sixth section we investigate CAMS/INV fluxes to help with the interpretation of our previous results. Finally, we summarize our results and discuss potential future uses of this method and suggestions for further research.

2 Data

2.1 Sentinel-5P/TROPOMI WFMD product

65 The Sentinel-5 Precursor (S5P) satellite was launched on 13 October 2017 and has since delivered high quality data from its only scientific instrument, TROPOMI, which is a nadir viewing passive grating imaging spectrometer. Combined with a near-polar, sun-synchronous orbit, the swath width of 2600 km provides daily global coverage. Due to the orbit geometry and swath overlap multiple observations per day are possible in the polar regions. The spatial resolution depends on the bands and is $5.5 \times 7 \text{ km}^2$ for the short-wave infrared (SWIR) band ($7 \times 7 \text{ km}^2$ before August 2019) (Ludewig, 2021). Methane is
70 retrieved from TROPOMI measurements of sunlight reflected by the Earth's surface and atmosphere in the SWIR wavelengths. We use the latest release of the WFMD product (v1.8) (Schneising et al., 2023), which includes processing improvements such as an increased polynomial degree (cubic instead of quadratic) and an updated digital elevation model to account for various localized topography related biases (Hachmeister et al., 2022). Furthermore, the machine-learning based quality filter in the post-processing is improved to further reduce scenes with residual clouds. We use data with a quality flag $qf=0$ (good) and
75 don't include data with $qf=1$ (potentially bad). The WFMD product includes measurements for solar zenith angles up to 75° . Data is currently available from 11.2017 to 02.2023, however, we exclude data from the commissioning phase (11.2017 to 04.2018).

2.2 CAMS global inversion-optimised greenhouse gas fluxes and concentrations (CAMS/INV)

The Copernicus Atmospheric Monitoring Service (CAMS) global inversion-optimised greenhouse gas fluxes and concentra-
80 tions dataset (CAMS/INV) provides model data for carbon dioxide, nitrous oxide and methane. The methane data is produced using the CAMS CH_4 Flux Inversion system (Segers et al., 2022), which is based on the TM5-4DVar inverse modeling system (Bergamaschi et al., 2010, 2013). We use release v22r1, where only ground-based observations from the NOAA network are used in the inversion (CAMS/INV-SRF) and release v21r1s, which includes satellite observations from the Greenhouse Gases Observing Satellite (GOSAT) in addition to ground-based observations (CAMS/INV-SRF-SAT). In our analysis we use the
85 total column dry-air mole fractions and surface fluxes of methane from this dataset. The data is provided on a $2^\circ \times 3^\circ$ grid from 1990 to 2022.

2.3 NOAA CH_4 Marine Boundary Layer Reference

The Marine Boundary Layer Reference (MBLR) is a 2-dimensional matrix (time vs. latitude) created from weekly air samples from the Cooperative Air Sampling Network (Dlugokencky et al., 2021), which is created for various long-lived trace gases by
90 NOAA-GML. The MBLR is created by first fitting the weekly data whereby the CH_4 level, seasonal component and short-term



variations are separated. For each time step (48 evenly distributed per year) the different stations give a latitudinal distribution of CH₄ which is then smoothed. The global mean is calculated by averaging the smoothed latitudinal distribution for each time step. A detailed explanation can be found on the NOAA website (NOAA, 2022).

2.4 Univ. Bremen C3S/CAMS satellite data (UB–C3S–CAMS)

95 Annual methane increases are published by the Copernicus Climate Change Service (C3S, C3S (2023c)) in the context of the European State of the Climate (ESOTC) assessment. Here we use data from the ESOTC 2022 (C3S, 2023d) climate indicator section (C3S, 2023a). The methane data as shown on that website are (i) time series of monthly values of the column-averaged mole fraction of atmospheric methane, XCH₄, as derived from satellite data, and (ii) annual mean methane growth rates including uncertainty estimates as derived from this time series. The XCH₄ time series corresponds to satellite data over land
100 in the latitude band 60° S – 60° N and covers the period January 2003 to December 2022. The underlying satellite XCH₄ data product for 2002–2021 is XCH₄_OBS4MIPS version 4.4 available from the Copernicus Climate Data Store (CDS,C3S (2023b)) website (C3S, 2018). A previous version of this data product is described in Reuter et al. (2020). This data set is extended using a year 2022 satellite-derived XCH₄ data product, generated for the Copernicus Atmosphere Monitoring Service (CAMS, CAMS (2023)) (see C3S (2023a) for details). The combined C3S/CAMS XCH₄ time series has been generated by
105 the University of Bremen (UB) and is used to derive annual mean methane growth rates for 2003–2022 using the method as described in Buchwitz et al. (2017), for XCO₂, which has later also been applied to XCH₄ (Reuter et al., 2020). This data set is in the following referred to as UB–C3S–CAMS data set.

3 Method

The method section is split into four parts. First we describe how the data is prepared for the DLM, meaning how we get from
110 single observations to a time-series we can fit our model to. Next we shortly introduce DLMs and provide information on the specific types of models we are using. In the third subsection we explain how we use an ensemble of DLMs and cross-validation to select the best model. Lastly, we describe how we estimate the bias related to imperfect satellite sampling.

3.1 Data preparation

Initially, the WFMD XCH₄ data product is gridded onto a 2° × 2° grid. For this we assign each measurement to a single
115 grid cell and calculate the weighted average of all measurements per cell. The measurements are weighted using the inverse measurement uncertainty to disadvantage measurements with high uncertainty. To account for inhomogeneities in spatial and temporal sampling of the data due to seasonal gaps and missing data (e.g. due to clouds) we apply the method described by Sofieva et al. (2014). This method quantifies the sampling distribution's inhomogeneity using a measure denoted as $0 \leq H \leq 1$, which is defined as a linear combination of the asymmetry A and entropy E of the data:

$$120 \quad H = \frac{1}{2}(A + (1 - E)) \quad (1)$$

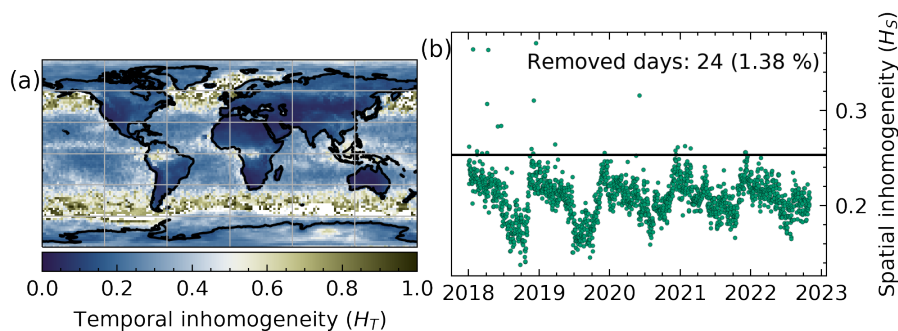


Figure 1. (a) Temporal inhomogeneity (H_T) for global XCH₄ WFMDv1.8 data between May 2018 and February 2023. Grid cells with $H_T > 0.5$ are omitted during analysis (b) Spatial inhomogeneity (H_S) for global XCH₄ WFMDv1.8 data. Days above the H_S threshold (black line) are omitted from analysis, the threshold is set by Eq. 2 which was empirically chosen.

Values close to zero indicate a homogeneous sampling distribution while values close to one indicate a very inhomogeneous distribution. Inaccurate estimates and spurious features can arise without accounting for this inhomogeneous sampling (Sofieva et al., 2014). We calculate the temporal inhomogeneity (H_T) for each grid cell, which tends to be higher in cells with sparse data coverage. We then filter cells with $H_T > 0.5$. This threshold value was chosen empirically to exclude cells in regions with known coverage problems, such as areas heavily affected by clouds (see Fig. 1). Next, we calculate the spatial inhomogeneity (H_S) within the designated sub-grid, such as a zonal band. We determine a limit, H_S^{lim} , as the median of H_S plus two standard deviations

$$H_S^{lim} = \tilde{H}_S + 2\sigma_{H_S} \quad (2)$$

and filter out days with $H_S > H_S^{lim}$. This filtering process removes days with highly inhomogeneous coverage. The equation for H_S^{lim} was empirically chosen and yields reliable limits for different sub-grids. Figure 1 illustrates the spatial and temporal inhomogeneity for global WFMDv1.8 data.

Finally, we compute the area-weighted average of the chosen sub-grid, generating a time series for further analysis. To mitigate sampling bias in the global average, we first average over longitudes and subsequently over latitudes. This approach assumes a faster mixing of background methane levels within zonal bands, while acknowledging greater latitudinal disparities. A more detailed description is given in Sec. 3.4.

CAMS/INV data is already provided on a grid and no inhomogeneity treatment is necessary. The time series are hence just calculated using the area-weighted average of the sub-grid. Since the DLM approach is based on the assumption that errors are present and normally distributed, we add a Gaussian noise with $\sigma = 0.5$ ppb to the time series.

3.2 Dynamic Linear Model fit

To extract information about the methane growth rate from the time-series we first calculate the underlying level, that is the smoothly changing background concentration without seasonal or short-term variation. While a simple approach, such as fitting



a polynomial plus a trigonometric function to model the seasonality, may be considered, it is insufficient due to the complex change in methane levels observed in historical records (Lan et al., 2023; C3S, 2023a). The use of a moving average is not suitable due to possible data gaps, especially for high latitude bands. Therefore, we employ dynamic linear models to fit the data, which allow for the trend (i.e. the slope of the level, the growth rate) to change over time and can deal with missing data. For the analysis of global methane growth we use AMIs, since they are already used by other sources (Dlugokencky, 2022; C3S, 2023a; Schneising et al., 2023) and therefore allow easy comparison of the results. AMIs are defined as the difference in methane level between the January 1st of two consecutive years, which is equal to the integrated growth rate over the same time span. For zonal bands we directly investigate the growth rate instead of AMIs (see Sec. 5 for a more detailed description).

A dynamic linear model is a regression model that can handle observations of varying accuracy, missing data, non-uniform sampling and non-stationary processes. It allows some of its parameters to change over time and directly models the observed variability using unobserved state variables (Laine, 2020). These properties allow the analysis of not only global but also zonal methane data, which can have higher uncertainties and more gaps, especially in the higher latitudes. Additionally, the direct modeling of the data allows the partition of the signal into different components, like an underlying level and seasonal component, which can prove advantageous beyond the scope of this paper. DLMs have been previously used to successfully model stratospheric ozone (Laine et al., 2014), methane from different GOSAT retrievals to investigate the seasonal cycle and trend (Kivimäki et al., 2019) and methane from ground-based remote sensing (Karppinen et al., 2020). For a detailed description of DLMs, including their formulation as a special case of a space-state model, we refer readers to Durbin and Koopman (2012) and Harvey (1990). For a more concise introduction to DLMs, we refer to Laine (2020). A DLM can be formulated as a special case of a space-state model, that is a model which consists of some unobserved components (represented by a state vector) and the observation vector. The evolution of the state vector and the relation between observation- and state-vector are modeled by a set of equations. If these equations are linear we have a so-called dynamic linear model. The DLM we use consists of three main components. First, a slowly changing background level, which captures the long-term trend of the methane concentration. Second, a seasonal component is included to model variations arising from seasonal cycles. This component enables variations in the phase and amplitude of the seasonal cycle to be accounted for. Third, an autoregressive component is incorporated to model noise and residual correlations in the data, accounting for short-term effects. Additionally, Gaussian noise can be included to model part of the errors. The ability of DLMs to capture changing components over time is achieved by modeling these changes as Gaussian random walks, allowing for smooth transitions and adjustments. The variances of these Gaussian random walks determine the overall variability of a certain parameter (e.g. trend). A detailed description of the model setup and the different DLM components can be found in Appendix A. Once the structure of the model is decided on, it can be brought into matrix form and the DLM consisting of the observation vector and the set of equations can then be solved using a Kalman Filter (Durbin and Koopman, 2012; Harvey, 1990; Laine, 2020). The Kalman Filter is a recursive algorithm that estimates the unobserved states of a system using observed data and model equations (Kalman, 1960). In general, the model parameters (e.g. variances) are not known beforehand and have to be determined. For this purpose, Maximum Likelihood Estimation (MLE) (Durbin and Koopman, 2012; Harvey, 1990) can be used. MLE is a statistical method that estimates the parameters of a model by maximizing the likelihood of the observed data given the model's assumptions. For the end-user various software exist

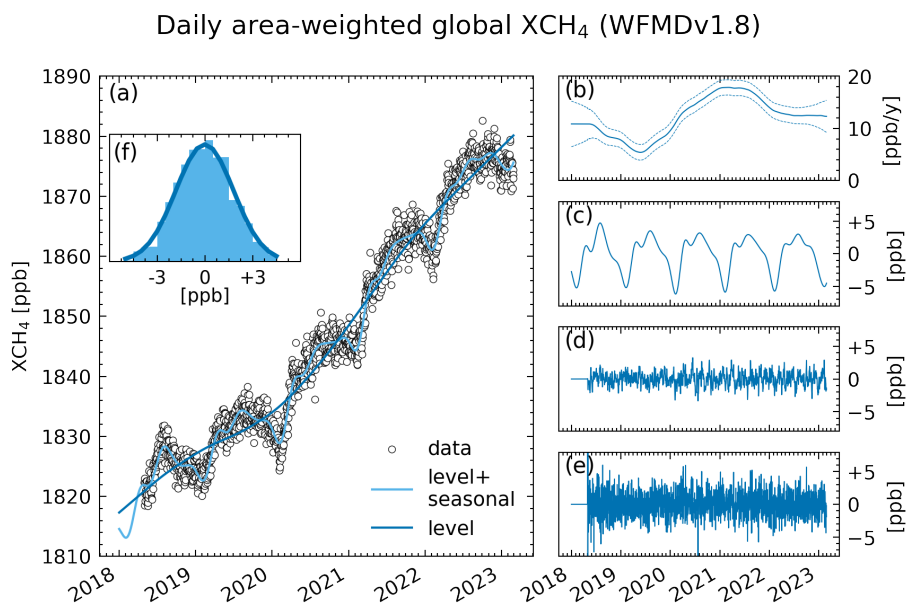


Figure 2. DLM fit for daily area-weighted global WFMDv1.8 data. (a) Shows the daily area-weighted global XCH₄ together with the level and level+seasonal components from the DLM fit (b) The trend or growth rate is the slope of the level, the dashed lines show the 1- σ uncertainty, (c) Shows the seasonal component which captures the seasonal cycle, (d) The AR(1) component captures residual correlations in the data, (e) The residual shows the difference between the fit and the data, (f) A histogram of the residual shows that it is roughly normally distributed.

which provide the implementation of this procedure, leaving only the model configuration open for the user. In our study we use the *UnobservedComponents* class of the python *statsmodel* package (Version 0.13.2, Perktold et al. (2023)). An overview of a DLM fit for globally averaged WFMD data can be seen in Fig. 2.

180 3.3 Ensemble approach and Cross Validation

The choice of model configuration is a non-trivial problem, which is impacted by prior knowledge, empirical testing and different quality measures. Prior knowledge may motivate the inclusion of a seasonal component, since the existence of a seasonality in atmospheric methane concentrations is known. Empirical testing can show that the inclusion of an autoregressive component is necessary, since the data contains residual short-term variations. And by quality measures we refer to measures that facilitate model selection, such as the mean squared error (MSE), which is defined as the mean of squared differences between model and data. Additionally, the DLM provides variances for each component which can be used to compare models; models with lower variances in the level and DLM seasonality (i.e. higher certainty & less variability) are preferable to models with high variances for these terms. To avoid the need for manual model selection, we employ an ensemble approach, fitting a range of DLMs to the data and automatically selecting the best model. The ensemble consists of different DLM configurations, with varying components, as described in Appendix A. Additionally, we perform cross-validation (CV) five folds for each DLM to



calculate an average mean squared error (AMSE). During CV, the DLM is trained on a portion of the data while leaving out another portion (the fold) for testing. The difference between the model fit and the fold is used to calculate the MSE, and the average MSE across all five folds per DLM provides the AMSE. Low AMSE values indicate a better model fit and help in selecting the best model for a given time-series. The final model selection is based on an aggregated score, defined as the sum of the AMSE, the variance of the level and the variance of the seasonal term:

$$S_{agg} = AMSE + \sigma_{level}^2 + \sigma_{seas}^2 \quad (3)$$

The inclusion of the variances ensures that the uncertainty of the level and seasonal components is considered in the selection criterion. This approach aims to select DLMs that provide good estimates of the underlying methane signal while avoiding overfitting and reliance on expert knowledge. Different methods and measure can be used for model selection and may yield different results. We want to emphasize that the problem of model selection is non-trivial and different approaches may be suitable for different data and use-cases. Here we select the model which yields the highest certainty fit of the level and seasonal component (i.e. the methane signal without noise) while avoiding overfitting and manual selection. Furthermore, we want to mention that in most cases the differences between all models in an ensemble are rather small with the best models producing approximately the same results. However, the use of a single DLM configuration for all zonal bands is not feasible due to the inherent differences in the seasonal signal for each zonal band. Additionally, an over-specified model can lead to high uncertainties in the resulting fit. To quantify the impact of model selection, we calculate a model selection bias σ_{model}^2 , which is included in the error budget of all AMIs and growth rates. For this we calculate AMIs or growth rates for all models in an ensemble and determine the weighted variance:

$$\sigma_{Model/AMI}^2 = \frac{\sum_i (AMI_{avg} - AMI_i)^2 \tilde{\sigma}_i^{-2}}{\sum_i \tilde{\sigma}_i^{-2}}; \quad \tilde{\sigma}_i^2 = \sigma_{avg}^2 + \sigma_i^2 \quad (4)$$

$$\sigma_{Model/trend}^2 = \frac{\sum_i (\nu_{avg} - \nu_i)^2 \tilde{\sigma}_i^{-2}}{\sum_i \tilde{\sigma}_i^{-2}}; \quad \tilde{\sigma}_i^2 = \sigma_{avg}^2 + \sigma_i^2 \quad (5)$$

where ν_i is the growth rate at time step i . The contribution of the model selection bias to the error budget can be seen in Tab. 1 for global AMIs and Tab. 2 for zonal growth rates. In case of global data, the contribution is small with $\sigma_{Model} < 1$ ppb but can be higher in specific cases. For example, this is the case for global AMIs in 2018, when only an incomplete time series is available. For zonal data, σ_{Model} varies between the bands and is on the range of 0.60–4.81 ppb/y.

3.4 Estimation of sampling bias

The spatio-temporal coverage of S5P XCH₄ data is limited mostly by cloud coverage, the polar nights and poorly reflective surfaces, while additional gaps may exist due to technical problems with the satellite platform. Additionally, the sampling distribution is not completely random but is influenced by the total land mass per latitudinal band and seasonal cloud coverage over the tropical and subtropical oceans. Therefore, we don't calculate the direct global average but perform initial longitudinal averaging to ensure equal weighting of all latitudes, which is crucial given the heterogeneous daily distribution of measurements. Here we investigate the systematic sampling bias due to polar nights, the total effect due to sampling and the effect



of our zonal first averaging approach. For this, we use CAMS/INV data (see Sec. 2.2) onto which we apply different filtering and averaging methods. We then compare AMIs calculated using different sampling and/or methods. To simulate the spatio-temporal pattern of S5P sampling, we created a daily mask from gridded WFMDv1.8 data and applied it to the model data. To only simulate the systematic effect of the polar nights, we created a daily mask using the average solar zenith angle (SZA) per grid cell with a cut-off value of 75° . The AMIs for CAMS/INV data were calculated using the same ensemble approach used for WFMD data. First, we investigate the effect of our zonal first averaging approach. Figure 3 shows AMIs calculated from CAMS/INV-SRF data using (i) no mask and standard averaging (ii) the S5P XCH₄ mask and standard averaging and (iii) the S5P XCH₄ mask and zonal first averaging. Using zonal first averaging the AMIs are closer to the AMIs derived from the complete data. This is especially visible for 2020, where the AMI is overestimated by roughly 3 ppb when using the standard averaging. Therefore, we use zonal first averaging for all calculations of globally averaged data. For zonally averaged data we use standard averaging. Next, we investigated the remaining bias due to sampling. For global data the biases are calculated by taking the squared difference between the AMI calculated on the complete data (without any sampling filtering) and the AMI calculated on the reduced CAMS/INV data. We calculate a separate bias for each year in our analysis.

$$\sigma_{Sampling}^2 = (AMI - AMI_{Sampling})^2 \quad (6)$$

$$\sigma_{SZA}^2 = (AMI - AMI_{SZA})^2 \quad (7)$$

Table 1 shows the resulting errors for global AMIs. The sampling bias is around 0.25 ppb for all fully available years and much higher for 2018 with 2.92 ppb. The contribution of the SZA related bias varies from year to year with a maximum value of 0.73 ppb in the year 2022. This variability might be related to the varying difference between the high- and mid-latitudes during the different years. When the difference between both is bigger, the masking of high-latitude regions is expected to have a larger effect on AMIs. For the analysis of zonal bands we calculate an error by taking the average squared difference between growth rates derived from the complete data and growth rates derived from the reduced CAMS/INV data:

$$\sigma_{Sampling/Zonal}^2 = \frac{1}{N} \sum_i^N (\nu_i - \nu_i^{Sampling})^2 \quad (8)$$

where ν_i is the growth rate at time step i and N is the total number of data points. The sampling errors for zonal growth rates are shown in Tab. 2. Higher sampling errors correlate clearly with regions of high temporal inhomogeneity which visualizes regions with challenging sampling conditions (see Fig. 1).

4 Comparison of different global annual methane increases

In this section, we discuss global AMIs calculated using WFMDv1.8 data from May 2018 to February 2023. The results are shown in Fig. 4. An overall, although non-linear, rise in methane level is observed between 2019 and 2022. The most significant change occurs from 2019 to 2020, with an increase from 6.89 ± 0.85 ppb to 14.40 ± 0.53 ppb. The highest AMI is observed in 2021, reaching 16.93 ± 0.67 ppb. The globally averaged XCH₄ has risen from 1817.32 ± 2.81 ppb at the beginning of 2018 to 1878.14 ± 0.16 ppb at the end of 2022.

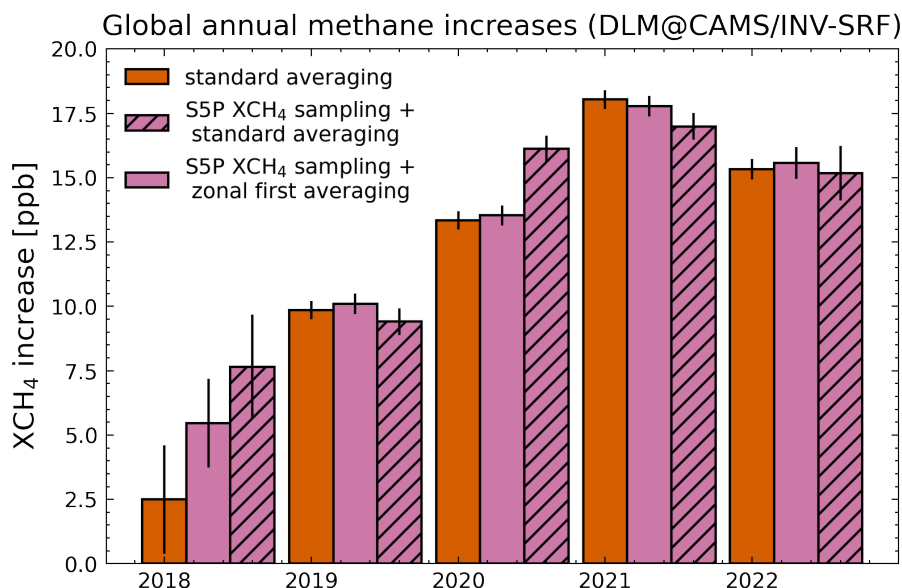


Figure 3. Global AMIs derived from CAMS/INV-SRF data using the complete data, the S5P sampled CAMS/INV-SRF data with standard averaging and the S5P sampled CAMS/INV-SRF data using our zonal-averaging first approach.

Table 1. Error budget for global AMIs. σ_{DLM} is the uncertainty provided by the DLM fit, σ_{Model} is the uncertainty from model selection and $\sigma_{Sampling}$ is the bias due to satellite sampling. All values show 1- σ uncertainties.

Year	2018 [†]	2019	2020	2021	2022
σ_{DLM}	1.70	0.40	0.39	0.39	0.49
σ_{Model}	3.22	0.71	0.32	0.48	0.35
$\sigma_{Sampling}$	2.96	0.25	0.19	0.26	0.25
$\sigma_{Sampling(SZA)}$	0.06	0.37	0.05	0.22	0.73
σ_{Total}	4.70	0.85	0.53	0.67	0.65

All values are in ppb, [†] 2018 only includes data starting 01.05.2018.

To validate our findings, we compared our results with AMIs determined by Schneising et al. (2023), the NOAA–GML (Dlugokencky, 2022), and data generated for the Copernicus Climate Change Service (C3S, 2023a). Additionally, we include AMIs derived using our DLM approach for monthly WFMDv1.8 data, NOAA–GML MBLR data and the UB–C3S–CAMS dataset. Table 3 and Fig. 6 provide a comparison of AMIs between 2018 and 2022. While absolute values may differ due to variations in data and methods, all AMIs exhibit the same qualitative trend. Differences are expected specifically for NOAA–GML AMIs, which are based on surface flask measurements rather than the total column observations used in the other calculations. To



Table 2. Sampling error for zonal growth rates. All values show 1- σ uncertainties.

Band	$\sigma_{Sampling}$	σ_{Model}
70–90° N	2.84	0.78
50–70° N	0.57	0.97
30–50° N	1.35	2.06
10–30° N	2.02	4.81
-10–10° N	0.93	2.81
10–30° S	0.86	1.93
30–50° S	2.33	0.60
50–70° S	3.49	3.95
70–90° S	1.82	2.02

All values are given in ppb/y

assess the impact of data and methodology, AMIs for the UB–C3S–CAMS and NOAA–GML datasets created using different methods can be compared. Our DLM based AMIs agree well with the calculations done for the C3S and by the NOAA–GML, indicating no significant differences due to the method used. An application of our DLM approach for the complete UB–C3S–CAMS and NOAA–GML MBLR data can be seen in Appendix B. Additionally, we used our DLM approach on monthly WFMDv1.8 data, to compare our method to the method used by Schneising et al. (2023), which also shows good agreement. Our results are therefore in good agreement with existing results from Schneising et al. (2023), the NOAA–GML (Lan et al., 2023) and the C3S (C3S, 2023a), when accounting for the difference in methodology or data used. No significant differences are found when comparing AMIs based on the same data or method. We also applied our approach to CAMS/INV data (see: 2.2), for which global AMIs can be seen in Fig. 5. The AMIs are in qualitative agreement and show the same structure over the 5-year period, however significant differences in absolute values are observed for 2019 and 2022. For 2019 the CAMS AMI seems to be in agreement with most other sources (see Tab. 3), while for 2022 CAMS is the clear outlier. The AMIs for 2020 and 2021 are the largest observed since NOAA began systematic records in 1983. The drivers contributing to these record increases have been the subject of recent debate and can be attributed to a rise in emissions, a reduction of the CH₄ sink, or a combination of both effects. According to the International Energy Agency (IEA) methane emissions from the energy sector decreased by approximately 10 % in 2020 (IEA, 2021). However, additional emissions due to reduced maintenance of landfills and oil and gas infrastructure can be expected according to Laughner et al. (2021), while McNorton et al. (2022) suggest that the effect of the global slowdown on anthropogenic CH₄ emissions is relatively small. Some studies propose that the reduction of the OH sink, caused by decreased emissions of nitrogen oxides during the COVID-19 pandemic, may explain part of the increase (Stevenson et al., 2022; Laughner et al., 2021; Peng et al., 2022; Qu et al., 2022; Feng et al., 2023). Specifically,

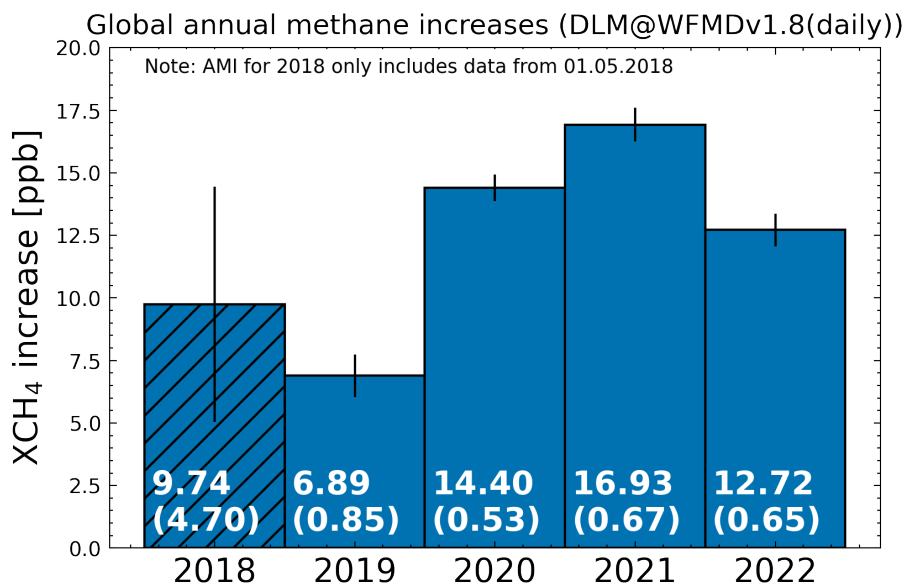


Figure 4. Global annual methane increases derived from Sentinel-5P/TROPOMI WFMDv1.8 data. The errorbars show the 1- σ uncertainty and include the DLM, sampling and model error.

Stevenson et al. (2022); Peng et al. (2022) suggest that approximately half of the increase can be attributed to this effect. Conversely, multiple other studies attribute the majority of the CH₄ increase in 2020 to the growth in wetland emissions (Qu et al., 2022; Feng et al., 2023, 2022; Zhang et al., 2023).

Table 3. Comparison of global AMIs using different data and methods. All errors represent 1- σ uncertainties.

	2018	2019	2020	2021	2022
DLM@WFMDv1.8 (daily)	9.74 ± 4.70 [†]	6.89 ± 0.85	14.40 ± 0.53	16.93 ± 0.67	12.72 ± 0.65
DLM@WFMDv1.8 (monthly)	6.56 ± 4.23 [†]	7.85 ± 0.98	14.39 ± 0.93	16.55 ± 0.94	12.65 ± 1.17
Schneising et al. (2023) @WFMDv1.8 (monthly)		7.80 ± 0.60	15.00 ± 1.00	16.40 ± 0.50	13.90 ± 0.60
NOAA–GML (Version 2023-07) @NOAA MBLR	8.70 ± 0.52	9.70 ± 0.60	15.20 ± 0.41	17.75 ± 0.47	13.95 ± 0.58
DLM@NOAA MBLR	9.37 ± 0.89	8.64 ± 0.77	15.97 ± 0.97	17.49 ± 1.26	
Buchwitz et al. (2017) @UB–C3S–CAMS	10.19 ± 1.96	9.00 ± 2.01	15.19 ± 2.09	17.09 ± 2.09	11.87 ± 2.77
DLM@UB–C3S–CAMS	10.15 ± 1.13	8.92 ± 1.30	15.77 ± 1.20	17.04 ± 1.05	11.46 ± 1.96
DLM@CAMS/INV–SURF	6.24 ± 0.97	9.86 ± 0.39	13.34 ± 0.38	18.04 ± 0.71	15.33 ± 0.48

All values are in ppb. Uncertainties reflect one standard deviation. [†] Larger error since only data starting with May 2018 was used

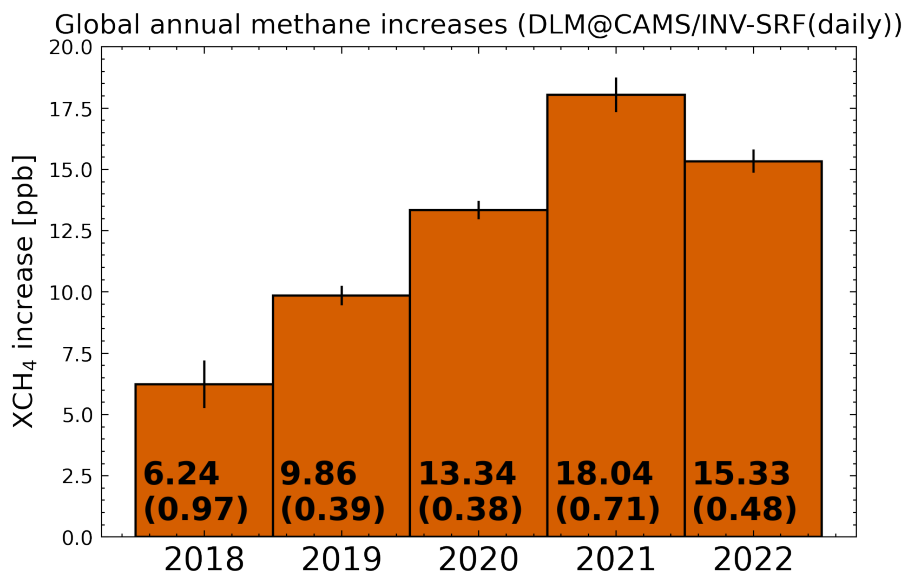


Figure 5. Global annual methane increases derived from CAMS global inversion-optimised greenhouse concentrations including only surface observations. The errorbars show the 1- σ uncertainty and include the DLM and model error, which are also shown in brackets.

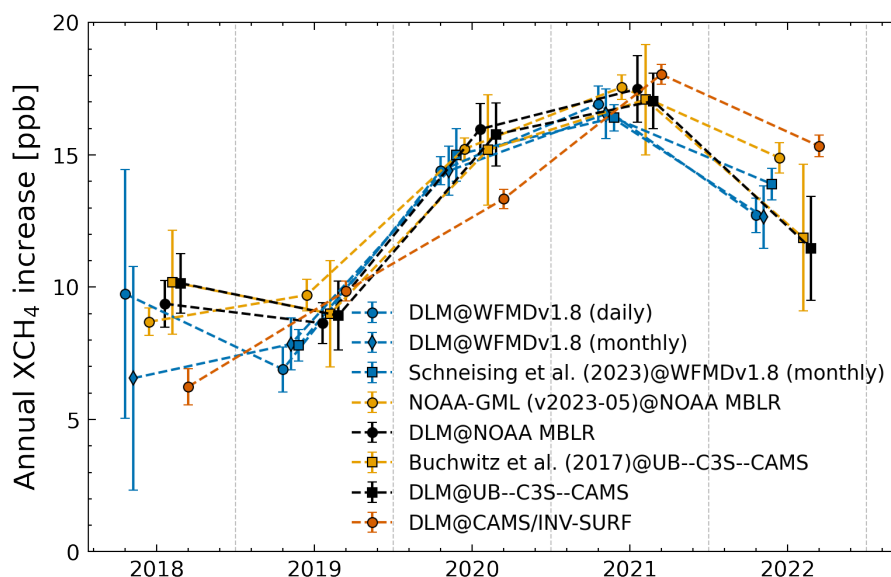


Figure 6. Comparison of global AMIs listed in Tab. 3. All errors represent 1- σ uncertainties.



5 Investigation of zonal methane growth rates

In addition to our global analysis, we also investigated 20° zonal bands. While the good spatio-temporal coverage of S5P XCH₄ might suggest that this would allow for the identification of zonal bands with anomalous methane increases using zonal AMIs, the atmospheric transport has to be considered. While longitudinal mixing occurs on timescales of a few weeks, meridional transport is slower, taking 1-2 months between mid-latitudes and tropics or polar regions and around a year between hemispheres (Jacob, 1999; Warneck, 1999). The relatively longer atmospheric lifetime of 9.1 years (Szopa et al., 2021) compared to the mixing times, therefore guarantees a relatively even latitudinal distribution of methane in the troposphere, where the main difference is driven by the uneven distribution of CH₄ sources (Warneck, 1999). Thus, we need to sample at about 1 year or less to observe differences between hemispheres and 1 month or less to observe differences within a hemisphere. The daily sampling of S5P is hence faster than meridional transport, however part of the temporal information gets lost when using AMIs which are obtained by integrating the growth rate over one year. Thus, we look at the growth rate, which is the trend component of our DLM fits, to obtain a better temporal resolution of the potential zonal signals. The results are shown in Fig. 7 and include growth rates derived from CAMS/INV-SRF data for comparison. The shown errors include the uncertainty gained from the DLM fit σ_{DLM} , the model selection error σ_{Model} and the sampling error $\sigma_{Sampling}$ (see Sec. 3.3 & 3.4). Growth rates are similar within a hemisphere, while differences between hemispheres are clearly visible. Additionally, no significant sub-annual variations in zonal growth rates are present. Both observations are in good agreement with the known atmospheric mixing times and indicate that our data currently allows for identification of inter-hemispheric differences while short-term variations between zonal bands are not detected. The high latitude band between 70°–90° is included for completeness, but shows no inter-annual variability. This may be due to a lack of real change in growth rates in this region and/or high uncertainties present in the data. The corresponding CAMS/INV-SRF growth rate indicates that the variability in growth rate is relatively small in this band, which supports the first point of our explanation. We therefore exclude this band from our following discussion. Hence, we mean bands between 10° S and 90° S when we speak of the Southern Hemisphere (SH) and bands between 10° S and 70° N when we speak of the Northern Hemisphere (NH). The band between 10° S and 10° N represents the boundary region and is close to the global background as can be seen in Fig. 8, which presents zonal growth rate anomalies. Zonal growth rate anomalies are defined as the difference between the zonal and the global growth rate for each band. Overall growth rates derived from WFMD data are close to growth rates derived from CAMS/INV-SRF data, with the strongest differences in the 50° S and 70° S band, which is also one of the most challenging bands to fit, due to the high cloud coverage and low landmass. The growth rates and the growth rate anomalies can be used to interpret the changes in global AMIs and allow the identification of hemispheres or zonal bands with anomalous growth rates. Differences between the hemispheres can be especially well seen in the zonal growth rate anomalies.

During 2019 a decrease in growth rates can be observed for the whole SH, while growth rates in the NH increased or stayed stable. For 2020 growth rates increase strongly from roughly 0 ppb/y to 20 ppb/y. The NH growth rates increase more slowly, except for the 50° N – 70° N band which exhibits a small decrease in growth rate. During 2021 most zonal growth rates move towards or around the global mean, with the strongest anomaly visible in the 10° N – 30° N band which shows some addi-

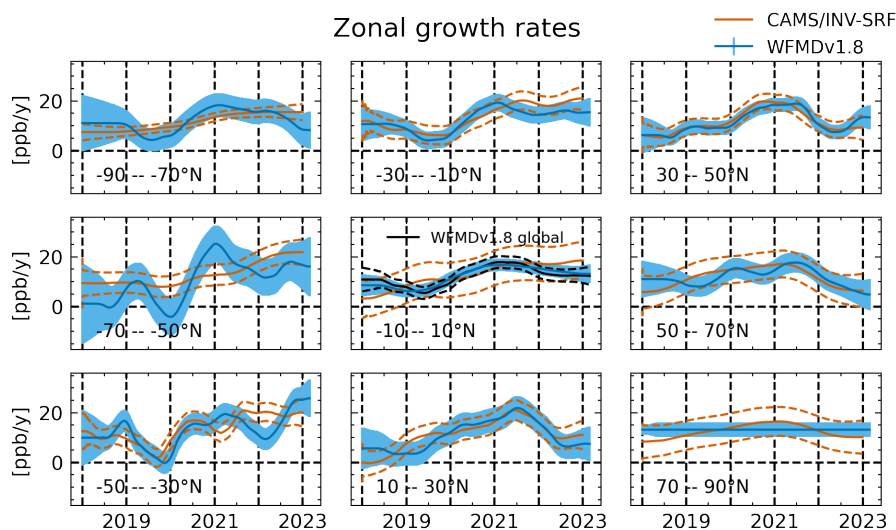


Figure 7. Zonal growth rates for 20° bands derived from Sentinel-5P/TROPOMI WFMDv1.8 data and CAMS/INV-SRF data. The errors show the 1- σ uncertainty.

315 tional increase in growth rate, which peaks mid of the year. During 2022 a clear difference between the hemispheres can be seen again, with a decrease of growth rates in the NH and an increase of growth rates in the SH. This difference is especially clear when looking at the zonal growth rate anomalies in Fig. 8. Recent studies, which discuss the record methane increases in 2020 and 2021 can help with interpreting the structure of zonal growth rates. Peng et al. (2022) employ an atmospheric inversion using ground-based data. They attribute the increase from 2019 to 2020 roughly equally to changes in the OH sink and an increase in wetland emissions located mainly in the NH. In contrast, studies based on the inversion of satellite data from the Japanese Greenhouse gases Observing SATellite (GOSAT) state that the majority of increase from 2019 to 2020 can be attributed to the African continent (Feng et al., 2023; Qu et al., 2022) with additional increases in tropical South America in 2021 (Feng et al., 2023). Our findings can thus be seen as aligning with recent studies by Feng et al. (2023); Qu et al. (2022). The increase in SH growth rates from 2019 to 2020 can be associated with increased wetland emissions. The rise in the NH 325 latitudinal bands during 2020 can be explained by the decreasing OH sink, primarily located in the NH (Peng et al., 2022; Feng et al., 2023). However, the continued increase in 2021 cannot be solely explained by the OH sink, as OH levels mostly recovered in that year according to Feng et al. (2023) and (Peng et al., 2022). It is likely that the ongoing increase is related to persistent wetland emissions Feng et al. (2023), as well as the return to pre-pandemic methane emissions from the energy sector in 2021 (IEA, 2023). Finally, the decrease of growth rates in the Northern and increase of growth rates in the SH during 330 2022 hasn't been discussed to our knowledge. Our results therefore indicate that the decrease in global AMI from 2021 to 2022 can be attributed to a reduced growth rate in the NH. We further investigate this in the next section.

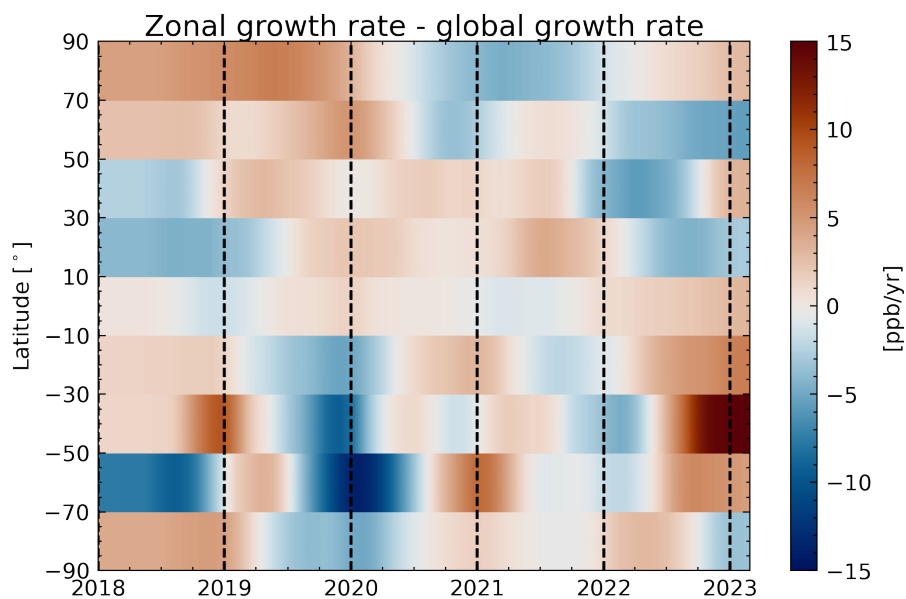


Figure 8. Zonal growth rate anomalies for 20° bands derived from Sentinel-5P/TROPOMI WFMDv1.8 data. The anomalies are defined as the difference between zonal and global growth rates.

6 CAMS/INV Fluxes

As mentioned before, zonal growth rates provide information about the change of methane concentration in a given zonal band, including changes in sources, sinks and transport patterns. These transport patterns would average out for global AMIs given a perfect coverage. Comparison of our global AMIs with global AMIs from other sources indicate, that the effect of transport related sampling biases seems to be limited. Therefore, changes in global AMIs can be attributed to the total source-sink balance of methane and not to changes in transport patterns. Whether this is also true for zonal growth rates is less clear, since transport effects are expected to be stronger especially within hemispheres. The similarity of zonal growth rates derived from WFMD and CAMS/INV data in Fig. 7, suggest that the structures observed in our zonal growth rates are not artifacts from sampling related biases. However, we cannot rule out transport effects from this comparison, meaning we can't clearly attribute changes in hemispheres or zonal bands over the years to a change in the source-sink balance. Hence, we also investigated the change of surface fluxes from CAMS/INV data between consecutive years. In Figure 9, 10 and 11 we present total, wetland and other fluxes for CAMS/INV-SRF data respectively. Additionally, rice and biomass burning fluxes exist, which are not shown here. The category of other fluxes includes all other anthropogenic emissions as well as oceans, wild animals, the soil sink and termites. Overall a great change in fluxes can be observed between all investigated years. The wetland flux difference between 2019 and 2020 indicate a strong increase in the NH as indicated by (Peng et al., 2022) as well as some increase in the SH wetlands as reported by (Feng et al., 2023) and (Qu et al., 2022). We expect the SH wetland fluxes to be underestimated as indicated by Feng et al. (2023) since the CAMS/INV-SRF data is only based on ground-based measurements from the NOAA

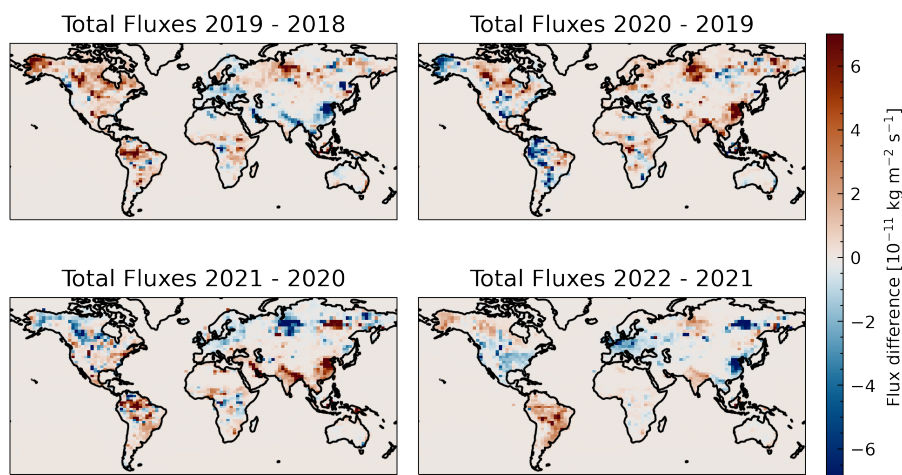


Figure 9. Difference between total surface fluxes from the CAMS/INV-SRF data.

network, similar to the inversion performed by Peng et al. (2022), due to the poor coverage in the tropics. Interestingly, wetland
350 fluxes from CAMS/INV-SRF-SAT data including satellite measurements from GOSAT show stronger SH wetland emissions
between 2019 and 2020 as shown in Figure 12. Additionally an increase in other fluxes occurs between 2019–2020 and 2020–
2021. In the first case these increases are mainly focused on China, while in the second case additional increases over the
Indian subcontinent can be seen. Between 2021 and 2022 a clear decrease of fluxes can be seen in large parts of the NH, while
strong increases can be observed over the whole of south America. The large decreases in the NH can be clearly attributed to
355 changes in the other fluxes, while the increase over south America seems to involve a combination of wetland and other fluxes.
This investigation of CAMS/INV fluxes indicates that the changes in zonal growth rates we observed both in WFMD and
CAMS/INV are not merely due to changes in transport patterns but correlate with changes in surface methane fluxes between
the years.

7 Conclusions

360 In this study, we presented a DLM based approach to calculate methane growth rates and AMIs from S5P/TROPOMI data.
We addressed sampling-related biases by comparing AMIs and growth rates derived from CAMS/INV data both with and
without S5P XCH₄ sampling. Further, we included a bias related to the model selection in our error budget. Our calculations
of global AMIs based on WFMDv1.8 data from 2018 to 2022 demonstrate good agreement with other AMIs. Additionally,
we separated the influence of the fitting method and the underlying data by applying our DLM approach to other datasets.
365 We show that using the same method or the same input data results in agreement within 1- σ between all AMIs (except for
CAMS/INV AMIs). Moreover, the consistency of AMIs derived from diverse datasets, such as ground-based data from NOAA
and total-column data from WFMDv1.8 and UB-C3S-CAMS, highlights the robustness of these various approaches. The

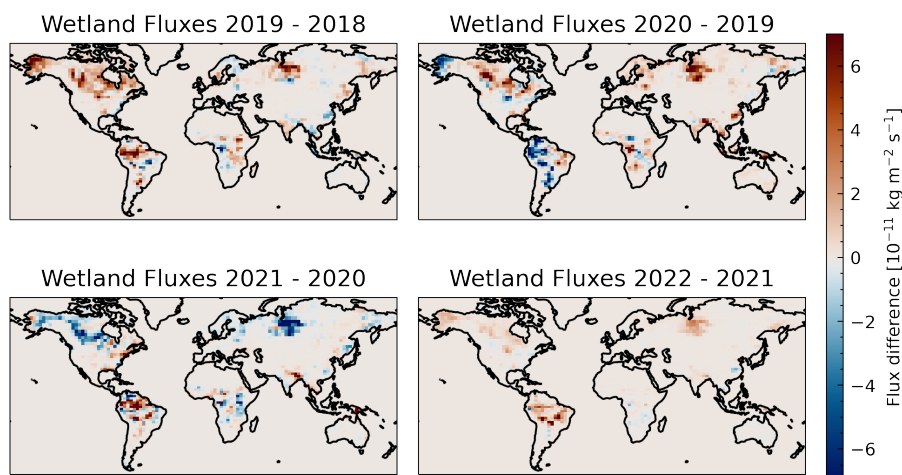


Figure 10. Difference between wetland surface fluxes from the CAMS/INV-SRF data.

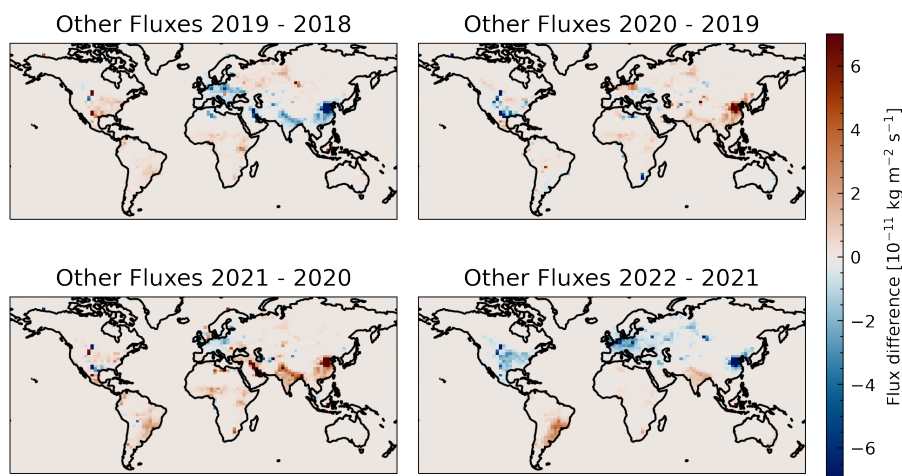


Figure 11. Difference between other surface fluxes from the CAMS/INV-SRF data.

record methane increase in 2020 and 2021 is therefore well documented using different data and methods. The underlying factors driving these increases, as discussed in Section 4, remain however a subject of debate. In addition to global AMIs we investigated growth rates for 20° zonal bands which provide spatial information to the global AMIs. We argue that this is possible due to (a) the faster zonal mixing in comparison to meridional mixing and (b) the faster satellite sampling in comparison to the meridional mixing times. Comparisons of zonal growth rates from S5P/TROPOMI data with growth rates from CAMS/INV-SRF data show good agreement and indicate that no significant sampling biases exist for zonal bands. Still we want to emphasize that meridional transport affects the zonal growth rates, meaning they don't only indicate changes in the sources and sinks of methane but might also show systematic changes in transport patterns. The zonal growth rates exhibit clear

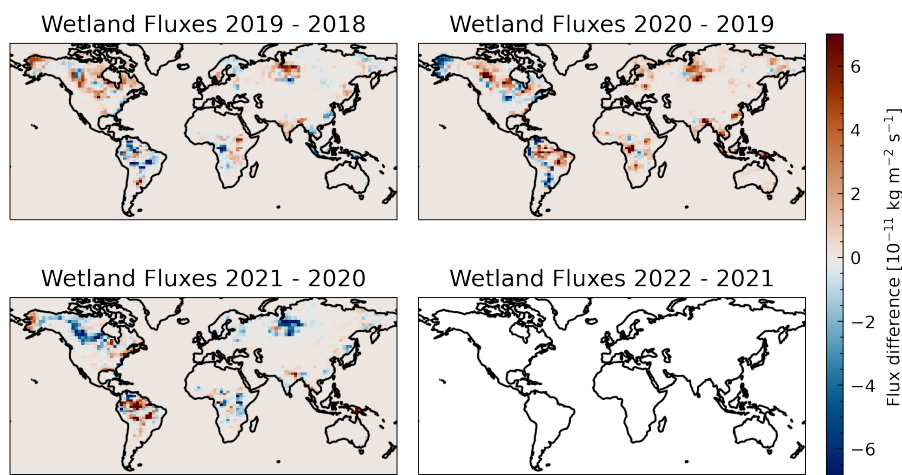


Figure 12. Difference between total surface fluxes from the CAMS/INV-SRF-SAT data. No Flux difference is available for 2022 - 2021, since the dataset currently ends in 2021.

differences between the hemispheres for 2019 and 2022, while growth rates are more similar for 2020 and 2021. Differences within a hemisphere are mostly smaller and no additional short-term variations are visible, which might reflect the well-mixed state of the atmosphere within a hemisphere. The low growth rates in the SH in 2019 and subsequent increases suggest a rise in atmospheric methane in that region, possibly driven by tropical wetland emissions according to Feng et al. (2023); Qu et al. (2022); Zhang et al. (2023). Other factors potentially contributing to these changes include variations in the OH sink due to pollutant reductions during the COVID-19 pandemic (Feng et al., 2023; Qu et al., 2022; Peng et al., 2022) and the changes in global methane emissions due to the COVID-19 pandemic and the subsequent recovery (IEA, 2021). We further investigated this inter-hemispheric differences by investigating the surface fluxes from CAMS/INV data, which are consistent with the derived zonal growth rates. The total surface fluxes show clear changes between the years, indicating that the changes in zonal growth rates are not only due to changes in transport patterns. The partition into wetland and other (mainly anthropogenic) fluxes allows further interpretation and shows reasonable qualitative agreement with findings reported by Feng et al. (2023); Qu et al. (2022); Peng et al. (2022). Most notably, the decrease in the global AMI in 2022 can be attributed to the decrease of other fluxes (which include mainly anthropogenic fluxes) in the NH, while wetland fluxes continue to rise in the SH.

In summary, our DLM-based approach allows for the calculation of growth rates or AMIs for global and zonal S5P/TROPOMI data. This approach is computationally inexpensive and allows for the constant integration of new data, enabling timely assessments of global methane concentration changes. Importantly, no prior information about the atmospheric state is required. We believe that our approach provides an additional valuable tool for investigating atmospheric methane concentrations, enabling the rapid identification of regions of interest, like the 2022 NH. Furthermore, our approach can be readily applied to other datasets facing similar challenges, such as inhomogeneous sampling, non-linear trends, and data gaps. For the 70°–90° N band our method failed to identify any changes in growth rate, however this result is in good agreement with the growth rates from



CAMS/INV-SRF data which themselves only show small variations. This indicates that (a) The small changes in growth rate could not be distinguished from the random variability in the data and (b) No anomalous increases in growth rate are visible for the northern high latitude regions. Future research could aim to improve this approach, especially for high latitude regions, to identify smaller changes in growth rates. To quantify the impact of meridional transport on zonal growth rates, the 2022 decrease in NH growth rates could be investigated in more detail and this approach be extended to include data sets of other atmospheric constituents. Data from future satellite mission, with lower uncertainties and increased data coverage, could further allow for the investigation of sub-annual changes in growth rates, which are presently not detectable. Finally, zonal growth rates of long-lived gases without any significant sources or sinks could possibly allow for the quantification of atmospheric transport patterns.

405 *Code and data availability.* CAMS global inversion-optimized greenhouse gas fluxes and concentrations are available from <https://ads.atmosphere.copernicus.eu/>. Sentinel-5P/TROPOMI WFMD data is available from https://www.iup.uni-bremen.de/carbon_ghg/products/tropomi_wfmd/. NOAA MBL data is available from <https://gml.noaa.gov/ccgg/mbl/>. Example code to recreate Fig. 4 (Global annual methane increases), including the gridding and processing of the data, is available under <https://doi.org/10.5281/zenodo.8178927>.

Appendix A: Model setup and ensemble size

410 The structure of our DLMs is informed by the basic assumption that the measured methane signal can be separated into a slowly changing background level, a seasonal component and noise term. This section closely follows the more detailed description in Durbin and Koopman (2012) and Harvey (1990). The level component μ_t can be described by the following formulas

$$\mu_{t+1} = \mu_t + \nu_t + \epsilon_{level}, \quad \epsilon_{level} \sim N(0, \sigma_{level}^2) \quad (A1)$$

$$\nu_{t+1} = \nu_t + \epsilon_{trend}, \quad \epsilon_{trend} \sim N(0, \sigma_{trend}^2) \quad (A2)$$

415 where ν_t is the trend (i.e. the slope or change of the level). Since we assume a smoothly changing level we allow the trend to change over time, which is modeled by a random walk with variance σ_{trend}^2 . Additionally we enforce a constraint of zero variance for the level to ensure that short-term fluctuations in the background level are not allowed:

$$\sigma_{level}^2 = 0 \quad (A3)$$

$$\sigma_{trend}^2 > 0 \quad (A4)$$

420 The seasonal part of the signal is modeled by a truncated Fourier-series with h harmonics:

$$\gamma_t = \sum_{j=1}^h \gamma_{jt} \quad (A5)$$



with

$$\gamma_{j,t+1} = \gamma_{jt} \cos(\lambda_j) + \gamma_{jt}^* \sin(\lambda_j) + \epsilon_{seas}, \quad \epsilon_{seas} \sim N(0, \sigma_{seas}^2), \quad \lambda_j = \frac{2\pi j}{s} \quad (\text{A6})$$

$$\gamma_{j,t+1}^* = -\gamma_{jt} \sin(\lambda_j) + \gamma_{jt}^* \cos(\lambda_j) + \epsilon_{seas}^*, \quad \epsilon_{seas}^* \sim N(0, \sigma_{seas}^2), \quad j = 1, \dots, h \quad (\text{A7})$$

425 where s describes the seasonality of the data, e.g. for monthly data $s = 12$ or for daily data $s = 365$ when modeling yearly patterns. The value of $s = 365.25$ can be used to account for leap years. We use $s = 365.2$ which is equal to the average number of days per year between 2018 and 2022. For $\sigma_{seas}^2 > 0$ the seasonal cycle is allowed to change over time. We allow values of $h \in \{1, 2, 3, 4\}$, to account for varying levels of complexity in the seasonal cycle. The motivation for this is twofold. Firstly, we want to only model the basic structure of the seasonal cycle and not the whole signal. Secondly, the inclusion of more harmonics
430 introduces further parameters which have to be estimated. This quickly leads to high uncertainties in the produced fit since not enough information is included in the data to account for the growing number of parameters. The noise term accounts for residual correlations as well as random Gaussian noise in the signal. This is achieved by including a serial dependence between the observations. An autoregressive noise of order n therefore includes a memory of the last n measurements. For $n = 1$ this $AR(1)$ term is

$$435 \quad \eta_{t+1} = \rho \eta_t + \epsilon_{AR(1)}, \quad \epsilon_{AR(1)} \sim N(0, \sigma_{AR(1)}^2), \quad \rho \in [0, 1] \quad (\text{A8})$$

which introduce the parameters ρ and $\sigma_{AR(1)}^2$ to the model. We confine our autoregressive component to the order of $n = 1$, which is enough to model the residual correlations in the data. Higher orders would introduce further parameters to be estimated and lead to a harder interpretability of the results. However, exclusion of the $AR(1)$ component leads to bad fits since the model fails to account for the data variability. An additional Gaussian noise can be included

$$440 \quad \epsilon_{irr}, \quad \epsilon_{irr} \sim N(0, \sigma_{irr}^2) \quad (\text{A9})$$

which we call *irregular* component. The complete signal can be then written as the sum of these components

$$y_t = \mu_t + \gamma_t + \eta_t + \epsilon_{irr} \quad (\text{A10})$$

The remaining tunable parameters are the variability of the seasonal term, the inclusion of a Gaussian error term and the number of harmonics which determine the size of the ensemble ($N = 2 \cdot 2 \cdot 4 = 16$). An overview of all parameters can be found in Tab.

445 A1.

Appendix B: Replication of complete NOAA GML & UB-C3S AMIs

To investigate the effect of the fitting method on AMIs we replicated AMIs calculated by the NOAA-GML and C3S in Fig. B1 and B2 respectively. Here we present the comparison for the whole available time range (subset of data can be seen in Tab. 3).



Table A1. DLM parameters.

Parameter	Description	Allowed range
σ_{level}^2	Variability of level	0
σ_{trend}^2	Variability of trend	$[0, \infty]^*$
σ_{seas}^2	Variability of seasonal cycle	0 or [†] $[0, \infty]^*$
ρ	Parameter of AR(1)	$[0, 1]^*$
$\sigma_{AR(1)}^2$	Variability of AR(1)	$[0, \infty]^*$
σ_{irr}^2	Variability of Gaussian error	0 or [†] $[0, \infty]^*$
h	Number of harmonics	$1 - 4^\dagger$

* determined by maximum likelihood estimation during DLM fit, [†] Different settings are part of ensemble

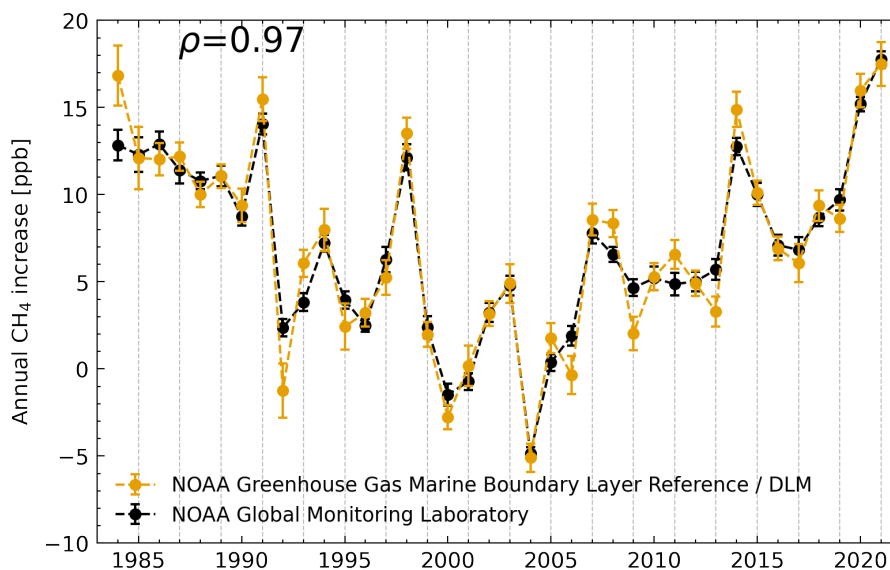


Figure B1. Comparison of global annual methane increases derived from the NOAA–GML MBLR data using different methods.

Appendix C: Global AMIs and zonal growth rates derived from CAMS global inversion-optimised greenhouse concentrations

450

Here we present global AMIs and zonal growth rates for CAMS/INV-SRF-SAT data which includes satellite measurements from GOSAT in its optimization (see Fig. C1 and C2).

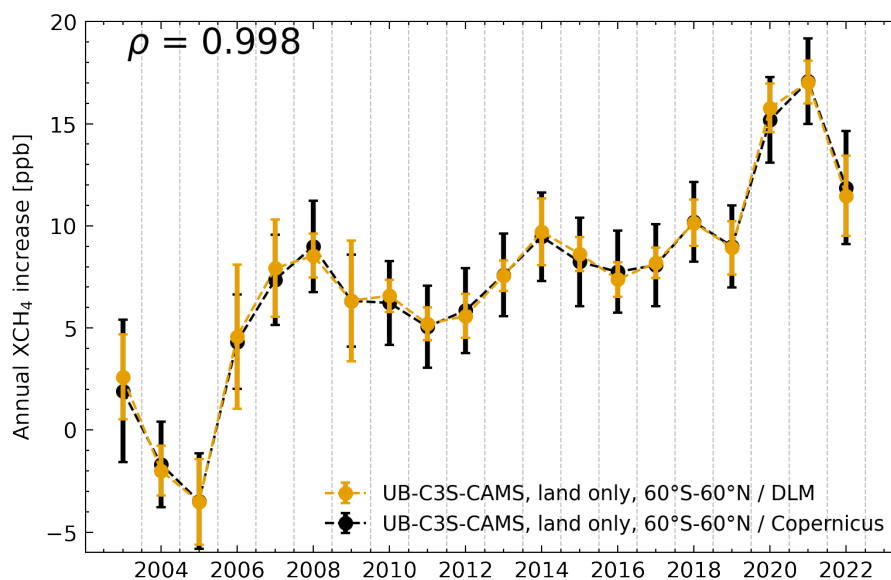


Figure B2. Comparison of global annual methane increases derived from C3S XCH₄_OBS4MIPS v4.4 data which is extended by CAMS NRT data after 2021 using different methods.

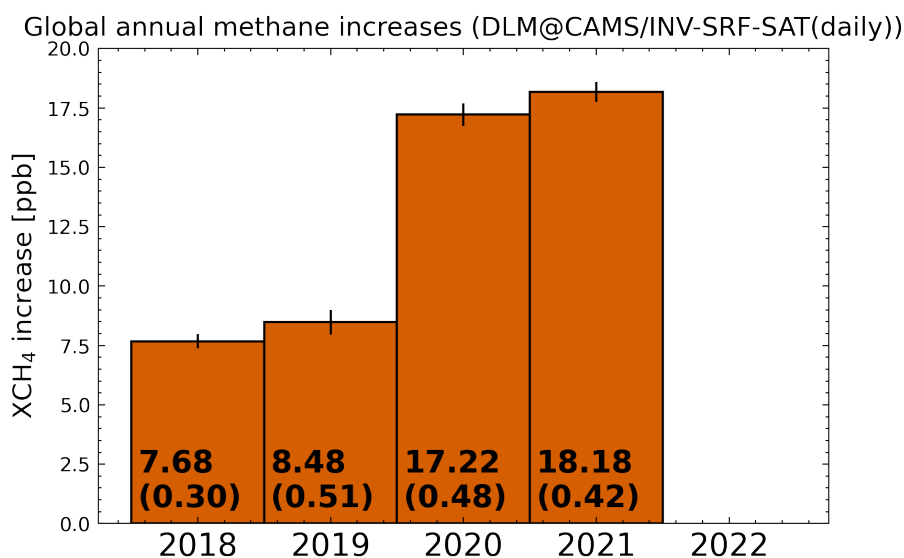


Figure C1. Global annual methane increases derived from CAMS global inversion-optimised greenhouse concentrations including both surface and satellite observations.

Author contributions. JH developed the methodology and conducted the formal analysis. OS, MB, JPB, JN and MB provided supervision and helped with the conceptualization. JH wrote the initial draft of this manuscript. All authors contributed to the final version of this

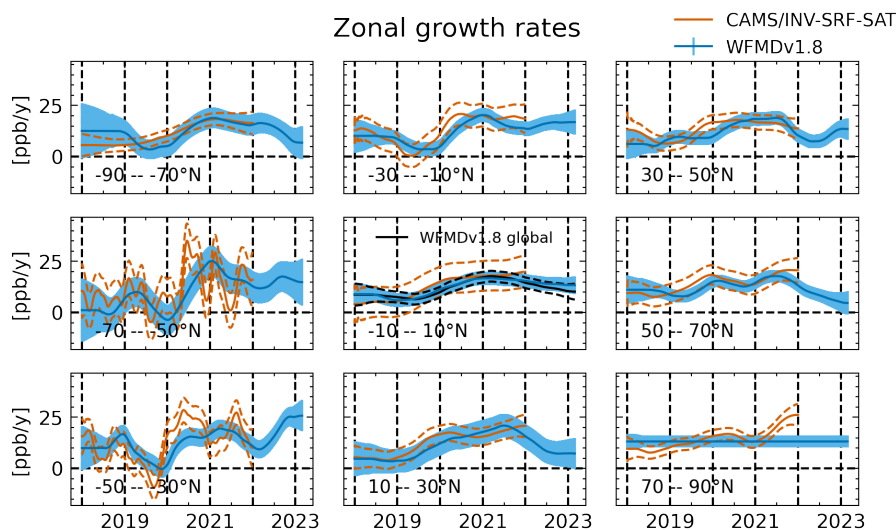


Figure C2. Zonal growth rates for 20° bands derived from Sentinel-5P/TROPOMI WfMDv1.8 data and CAMS/INV-SRF-SAT data. The errors show the 1- σ uncertainty.

Competing interests. The authors declare that they have no conflict of interest.

Disclaimer. Neither the European Commission nor ECMWF is responsible for any use that may be made of the information it contains.

Acknowledgements. Contains modified Copernicus Atmosphere Monitoring Service information (2018–2022). This publication contains modified Copernicus Sentinel data (2018–2023). Sentinel-5 Precursor is an ESA mission implemented on behalf of the European Commission. The TROPOMI payload is a joint development by the ESA and the Netherlands Space Office (NSO). The Sentinel-5 Precursor ground-segment development has been funded by the ESA and with national contributions from the Netherlands, Germany, and Belgium. The pre-operational TROPOMI data processing was carried out on the Dutch national e-infrastructure with the support of SURF Cooperative. Scientific color maps (Crameri, 2021) are used in this study to prevent visual distortion of data and exclusion of readers with color-vision deficiencies (Crameri et al., 2020).

Financial support. This project is funded through the University of Bremen, as part of the junior research group ‘Greenhouse gases in the Arctic’. We gratefully acknowledge the funding by the Deutsche Forschungsgemeinschaft (DFG, German Research Foundation) – Projektnummer 268020496 – TRR 172, within the Transregional Collaborative Research Center ‘Arctic Amplification: Climate Relevant Atmospheric and SurfaCe Processes, and Feedback Mechanisms (AC)³’. The research leading to the presented results received funding from the European Space Agency (ESA) via the projects GHG-CCI+ and MethaneCAMP (ESA contract nos. 4000126450/19/I-NB and



470 4000137895/22/I-AG) and from the German Ministry of Education and Research (BMBF) within its project ITMS via grant 01 LK2103A.
The TROPOMI/WFMD version 1.8 data have been generated using funding from ESA (GHG-CCI and MethaneCAMP projects). The
TROPOMI/WFMD retrievals presented here were performed on HPC facilities of the IUP, University of Bremen, funded under DFG/FUGG
grant nos. INST 144/379-1 and INST 144/493-1. Part of the AMIs presented were generated for Copernicus ESOTC 2022 (<https://climate.copernicus.eu/climate-indicators/greenhouse-gas-concentrations>) funded by EU Copernicus Climate Change Service via project C3S2_
475 312a_Lot2.



References

- Arias, P., Bellouin, N., Coppola, E., Jones, R., Krinner, G., Marotzke, J., Naik, V., Palmer, M., Plattner, G.-K., Rogelj, J., Rojas, M., Sillmann, J., Storelvmo, T., Thorne, P., Trewin, B., Achuta Rao, K., Adhikary, B., Allan, R., Armour, K., Bala, G., Barimalala, R., Berger, S., Canadell, J., Cassou, C., Cherchi, A., Collins, W., Collins, W., Connors, S., Corti, S., Cruz, F., Dentener, F., Dereczynski, C., Di Luca, A., Diongue Niang, A., Doblus-Reyes, F., Dosio, A., Douville, H., Engelbrecht, F., Eyring, V., Fischer, E., Forster, P., Fox-Kemper, B., Fuglested, J., Fyfe, J., Gillett, N., Goldfarb, L., Gorodetskaya, I., Gutierrez, J., Hamdi, R., Hawkins, E., Hewitt, H., Hope, P., Islam, A., Jones, C., Kaufman, D., Kopp, R., Kosaka, Y., Kossin, J., Krakovska, S., Lee, J.-Y., Li, J., Mauritsen, T., Maycock, T., Meinshausen, M., Min, S.-K., Monteiro, P., Ngo-Duc, T., Otto, F., Pinto, I., Pirani, A., Raghavan, K., Ranasinghe, R., Ruane, A., Ruiz, L., Sallée, J.-B., Samset, B., Sathyendranath, S., Seneviratne, S., Sörensson, A., Szopa, S., Takayabu, I., Tréguier, A.-M., van den Hurk, B., Vautard, R., von Schuckmann, K., Zaehle, S., Zhang, X., and Zickfeld, K.: Technical Summary, in: *Climate Change 2021: The Physical Science Basis. Contribution of Working Group I to the Sixth Assessment Report of the Intergovernmental Panel on Climate Change*, edited by Masson-Delmotte, V., Zhai, P., Pirani, A., Connors, S., Péan, C., Berger, S., Caud, N., Chen, Y., Goldfarb, L., Gomis, M., Huang, M., Leitzell, K., Lonnoy, E., Matthews, J., Maycock, T., Waterfield, T., Yelekçi, O., Yu, R., and Zhou, B., p. 33-144, Cambridge University Press, Cambridge, United Kingdom and New York, NY, USA, <https://doi.org/10.1017/9781009157896.002>, type: Book Section, 2021.
- Basu, S., Lan, X., Dlugokencky, E., Michel, S., Schwietzke, S., Miller, J. B., Bruhwiler, L., Oh, Y., Tans, P. P., Apadula, F., Gatti, L. V., Jordan, A., Necki, J., Sasakawa, M., Morimoto, S., Di Iorio, T., Lee, H., Arduini, J., and Manca, G.: Estimating Emissions of Methane Consistent with Atmospheric Measurements of Methane and $\delta^{13}\text{C}$ of Methane, *Atmospheric Chemistry and Physics Discussions*, 2022, 1–38, <https://doi.org/10.5194/acp-2022-317>, 2022.
- Bergamaschi, P., Krol, M., Meirink, J. F., Dentener, F., Segers, A., van Aardenne, J., Monni, S., Vermeulen, A. T., Schmidt, M., Ramonet, M., Yver, C., Meinhardt, F., Nisbet, E. G., Fisher, R. E., O'Doherty, S., and Dlugokencky, E. J.: Inverse modeling of European CH₄ emissions 2001–2006, *Journal of Geophysical Research: Atmospheres*, 115, <https://doi.org/10.1029/2010JD014180>, _eprint: <https://onlinelibrary.wiley.com/doi/pdf/10.1029/2010JD014180>, 2010.
- Bergamaschi, P., Houweling, S., Segers, A., Krol, M., Frankenberg, C., Scheepmaker, R. A., Dlugokencky, E., Wofsy, S. C., Kort, E. A., Sweeney, C., Schuck, T., Brenninkmeijer, C., Chen, H., Beck, V., and Gerbig, C.: Atmospheric CH₄ in the first decade of the 21st century: Inverse modeling analysis using SCIAMACHY satellite retrievals and NOAA surface measurements, *Journal of Geophysical Research: Atmospheres*, 118, 7350–7369, <https://doi.org/10.1002/jgrd.50480>, _eprint: <https://onlinelibrary.wiley.com/doi/pdf/10.1002/jgrd.50480>, 2013.
- Buchwitz, M., Schneising, O., Reuter, M., Heymann, J., Krautwurst, S., Bovensmann, H., Burrows, J. P., Boesch, H., Parker, R. J., Somkuti, P., Detmers, R. G., Hasekamp, O. P., Aben, I., Butz, A., Frankenberg, C., and Turner, A. J.: Satellite-derived methane hotspot emission estimates using a fast data-driven method, *Atmospheric Chemistry and Physics*, 17, 5751–5774, <https://doi.org/10.5194/acp-17-5751-2017>, publisher: Copernicus GmbH, 2017.
- C3S: Methane data from 2002 to present derived from satellite observations, <https://doi.org/10.24381/CDS.B25419F8>, 2018.
- C3S: Climate Indicators - Greenhouse gas concentrations, <https://climate.copernicus.eu/climate-indicators/greenhouse-gas-concentrations>, 2023a.
- C3S: Climate Data Store, <https://cds.climate.copernicus.eu#!/home>, 2023b.
- C3S: Copernicus Climate Change Service, <https://climate.copernicus.eu/>, 2023c.
- C3S: European State of the Climate 2022 | Copernicus, <https://climate.copernicus.eu/esotc/2022>, 2023d.



- CAMS: Copernicus Atmosphere Monitoring Service, <https://atmosphere.copernicus.eu/>, 2023.
- Cooper, M. J., Martin, R. V., Hammer, M. S., Levelt, P. F., Veefkind, P., Lamsal, L. N., Krotkov, N. A., Brook, J. R., and McLinden, C. A.:
515 Global fine-scale changes in ambient NO₂ during COVID-19 lockdowns, *Nature*, 601, 380–387, <https://doi.org/10.1038/s41586-021-04229-0>, number: 7893 Publisher: Nature Publishing Group, 2022.
- Crameri, F.: Scientific colour maps, <https://doi.org/10.5281/zenodo.5501399>, 2021.
- Crameri, F., Shephard, G. E., and Heron, P. J.: The misuse of colour in science communication, *Nature Communications*, 11, 5444,
<https://doi.org/10.1038/s41467-020-19160-7>, 2020.
- 520 Dlugokencky, E.: Trends in Atmospheric Methan, https://www.gml.noaa.gov/ccgg/trends_ch4/, last access: 20.09.2022, 2022.
- Dlugokencky, E. J., Lan, X., Crotwell, A., Thoning, K., and Crotwell, M.: Atmospheric Methane Dry Air Mole Fractions from the NOAA
ESRL Carbon Cycle Cooperative Global Air Sampling Network, ftp://aftp.cmdl.noaa.gov/data/trace_gases/ch4/flask/surface/, 2021.
- Durbin, J. and Koopman, S. J.: Time Series analysis by state space methods, Second Edition, Oxford University press, 2012.
- Feng, L., Palmer, P. I., Zhu, S., Parker, R. J., and Liu, Y.: Tropical methane emissions explain large fraction of recent changes in global
525 atmospheric methane growth rate, *Nature Communications*, 13, 1378, <https://doi.org/10.1038/s41467-022-28989-z>, 2022.
- Feng, L., Palmer, P. I., Parker, R. J., Lunt, M. F., and Bösch, H.: Methane emissions are predominantly responsible for record-breaking
atmospheric methane growth rates in 2020 and 2021, *Atmospheric Chemistry and Physics*, 23, 4863–4880, <https://doi.org/10.5194/acp-23-4863-2023>, 2023.
- Gulev, S., Thorne, P., Ahn, J., Dentener, F., Domingues, C., Gerland, S., Gong, D., Kaufman, D., Nnamchi, H., Quaas, J., Rivera, J., Sathyendranath, S., Smith, S., Trewin, B., von Schuckmann, K., and Vose, R.: Changing State of the Climate System, in: *Climate Change 2021: The Physical Science Basis. Contribution of Working Group I to the Sixth Assessment Report of the Intergovernmental Panel on Climate Change*, edited by Masson-Delmotte, V., Zhai, P., Pirani, A., Connors, S., Péan, C., Berger, S., Caud, N., Chen, Y., Goldfarb, L., Gomis, M., Huang, M., Leitzell, K., Lonnoy, E., Matthews, J., Maycock, T., Waterfield, T., Yelekçi, O., Yu, R., and Zhou, B., pp. 287–422, Cambridge University Press, Cambridge, United Kingdom and New York, NY, USA, <https://doi.org/10.1017/9781009157896.004>, type: Book
530 Section, 2021.
- Hachmeister, J., Schneising, O., Buchwitz, M., Lorente, A., Borsdorff, T., Burrows, J. P., Notholt, J., and Buschmann, M.: On the influence
of underlying elevation data on Sentinel-5 Precursor TROPOMI satellite methane retrievals over Greenland, *Atmospheric Measurement
Techniques*, 15, 4063–4074, <https://doi.org/10.5194/amt-15-4063-2022>, 2022.
- Harvey, A. C.: *Forecasting, Structural Time Series Models and the Kalman Filter*, Cambridge University Press,
540 <https://doi.org/10.1017/CBO9781107049994>, 1990.
- Hugelius, G., Strauss, J., Zubrzycki, S., Harden, J. W., Schuur, E. A. G., Ping, C.-L., Schirmermeister, L., Grosse, G., Michaelson, G. J., Koven, C. D., O'Donnell, J. A., Elberling, B., Mishra, U., Camill, P., Yu, Z., Palmtag, J., and Kuhry, P.: Estimated stocks of circumpolar permafrost carbon with quantified uncertainty ranges and identified data gaps, *Biogeosciences*, 11, 6573–6593, <https://doi.org/10.5194/bg-11-6573-2014>, 2014.
- 545 IEA: Methane Tracker 2021, <https://www.iea.org/reports/methane-tracker-2021>, license: CC BY 4.0, 2021.
- IEA: Global Methane Tracker 2022 – Analysis, <https://www.iea.org/reports/global-methane-tracker-2022>, 2023.
- Jacob, D. J.: *Introduction to Atmospheric Chemistry*, Princeton University Press, <https://doi.org/10.1515/9781400841547>, publication Title: *Introduction to Atmospheric Chemistry*, 1999.
- Kalman, R. E.: A New Approach to Linear Filtering and Prediction Problems, *Journal of Basic Engineering*, 82, 35–45,
550 <https://doi.org/10.1115/1.3662552>, 1960.



- Karppinen, T., Lamminpää, O., Tukiainen, S., Kivi, R., Heikkinen, P., Hatakka, J., Laine, M., Chen, H., Lindqvist, H., and Tamminen, J.: Vertical Distribution of Arctic Methane in 2009–2018 Using Ground-Based Remote Sensing, *Remote Sensing*, 12, 917, <https://doi.org/10.3390/rs12060917>, number: 6 Publisher: Multidisciplinary Digital Publishing Institute, 2020.
- 555 Kivimäki, E., Lindqvist, H., Hakkarainen, J., Laine, M., Sussmann, R., Tsuruta, A., Detmers, R., Deutscher, N. M., Dlugokencky, E. J., Hase, F., Hasekamp, O., Kivi, R., Morino, I., Notholt, J., Pollard, D. F., Roehl, C., Schneider, M., Sha, M. K., Velasco, V. A., Warneke, T., Wunch, D., Yoshida, Y., and Tamminen, J.: Evaluation and Analysis of the Seasonal Cycle and Variability of the Trend from GOSAT Methane Retrievals, *Remote Sensing*, 11, 882, <https://doi.org/10.3390/rs11070882>, number: 7 Publisher: Multidisciplinary Digital Publishing Institute, 2019.
- Laine, M.: Introduction to Dynamic Linear Models for Time Series Analysis, in: *Geodetic Time Series Analysis in Earth Sciences*, pp. 560 139–156, Springer International Publishing, Cham, https://doi.org/10.1007/978-3-030-21718-1_4, 2020.
- Laine, M., Latva-Pukkila, N., and Kyrölä, E.: Analysing time-varying trends in stratospheric ozone time series using the state space approach, *Atmospheric Chemistry and Physics*, 14, 9707–9725, <https://doi.org/10.5194/acp-14-9707-2014>, 2014.
- Lan, X., Basu, S., Schwietzke, S., Bruhwiler, L. M. P., Dlugokencky, E. J., Michel, S. E., Sherwood, O. A., Tans, P. P., Thoning, K., Etiope, G., Zhuang, Q., Liu, L., Oh, Y., Miller, J. B., Pétron, G., Vaughn, 565 B. H., and Crippa, M.: Improved Constraints on Global Methane Emissions and Sinks Using $\delta^{13}\text{C}\text{-CH}_4$, *Global Biogeochemical Cycles*, 35, e2021GB007000, <https://doi.org/https://doi.org/10.1029/2021GB007000>, [_eprint: https://agupubs.onlinelibrary.wiley.com/doi/pdf/10.1029/2021GB007000](https://agupubs.onlinelibrary.wiley.com/doi/pdf/10.1029/2021GB007000), 2021.
- Lan, X., Thoning, K., and Dlugokencky, E. J.: Trends in globally-averaged CH_4 , N_2O , and SF_6 determined from NOAA Global Monitoring Laboratory measurements. Version 2023-07, <https://doi.org/10.15138/P8XG-AA10>, 2023.
- 570 Laughner, J. L., Neu, J. L., Schimel, D., Wennberg, P. O., Barsanti, K., Bowman, K. W., Chatterjee, A., Croes, B. E., Fitzmaurice, H. L., Henze, D. K., Kim, J., Kort, E. A., Liu, Z., Miyazaki, K., Turner, A. J., Anenberg, S., Avise, J., Cao, H., Crisp, D., de Gouw, J., Eldering, A., Fyfe, J. C., Goldberg, D. L., Gurney, K. R., Hasheminassab, S., Hopkins, F., Ivey, C. E., Jones, D. B. A., Liu, J., Lovenduski, N. S., Martin, R. V., McKinley, G. A., Ott, L., Poulter, B., Ru, M., Sander, S. P., Swart, N., Yung, Y. L., and Zeng, Z.-C.: Societal shifts due to 575 COVID-19 reveal large-scale complexities and feedbacks between atmospheric chemistry and climate change, *Proceedings of the National Academy of Sciences*, 118, e2109481 118, <https://doi.org/10.1073/pnas.2109481118>, publisher: Proceedings of the National Academy of Sciences, 2021.
- Ludwig, A.: S5P Mission Performance Centre Level 1b Readme, <https://sentinels.copernicus.eu/documents/247904/3541451/Sentinel-5P-Level-1b-Product-Readme-File.pdf/a89d82ce-7414-43e6-ac77-0c371ed1b096>, 2021.
- 580 McNorton, J., Bousserez, N., Agustí-Panareda, A., Balsamo, G., Cantarello, L., Engelen, R., Huijnen, V., Inness, A., Kipling, Z., Parrington, M., and Ribas, R.: Quantification of methane emissions from hotspots and during COVID-19 using a global atmospheric inversion, *Atmospheric Chemistry and Physics*, 22, 5961–5981, <https://doi.org/10.5194/acp-22-5961-2022>, 2022.
- NOAA: NOAA/GML calculation of global means, <https://gml.noaa.gov/ccgg/mbl/mbl.html>, 2022.
- Peng, S., Lin, X., Thompson, R. L., Xi, Y., Liu, G., Hauglustaine, D., Lan, X., Poulter, B., Ramonet, M., Saunio, M., Yin, Y., Zhang, Z., Zheng, B., and Ciais, P.: Wetland emission and atmospheric sink changes explain methane growth in 2020, *Nature*, 612, 477–482, 585 <https://doi.org/10.1038/s41586-022-05447-w>, number: 7940 Publisher: Nature Publishing Group, 2022.
- Perktold, J., Skipper Seabold, Sheppard, K., ChadFulton, Kerby Shedden, Jbrockmendel, J-Grana6, Quackenbush, P., Arel-Bundock, V., McKinney, W., Langmore, I., Baker, B., Gommers, R., Yogabonito, S-Scherrer, Zhurko, E., Brett, M., Giampieri, E., Yichuan Liu, Mill-



- man, J., Hobson, P., Vincent, Roy, P., Augspurger, T., Tvanzyl, Alexbr, Hartley, T., Perez, F., Tamiya, Y., and Halchenko, Y.: statsmodel-
s/statsmodels: Release 0.14.0, <https://doi.org/10.5281/ZENODO.593847>, 2023.
- 590 Plaza, C., Pegoraro, E., Bracho, R., Celis, G., Crummer, K. G., Hutchings, J. A., Hicks Pries, C. E., Mauritz, M., Natali, S. M., Salmon,
V. G., Schädel, C., Webb, E. E., and Schuur, E. A. G.: Direct observation of permafrost degradation and rapid soil carbon loss in tundra,
Nature Geoscience, 12, 627–631, <https://doi.org/10.1038/s41561-019-0387-6>, 2019.
- Qu, Z., Jacob, D. J., Zhang, Y., Shen, L., Varon, D. J., Lu, X., Scarpelli, T., Bloom, A., Worden, J., and Parker, R. J.: Attribution of
the 2020 surge in atmospheric methane by inverse analysis of GOSAT observations, Environmental Research Letters, 17, 094003,
595 <https://doi.org/10.1088/1748-9326/ac8754>, publisher: IOP Publishing, 2022.
- Reuter, M., Buchwitz, M., Schneising, O., Noël, S., Bovensmann, H., Burrows, J. P., Boesch, H., Di Noia, A., Anand, J., Parker, R. J.,
Somkuti, P., Wu, L., Hasekamp, O. P., Aben, I., Kuze, A., Suto, H., Shiomi, K., Yoshida, Y., Morino, I., Crisp, D., O'Dell, C. W., Notholt, J.,
Petri, C., Warneke, T., Velazco, V. A., Deutscher, N. M., Griffith, D. W. T., Kivi, R., Pollard, D. F., Hase, F., Sussmann, R., Té, Y. V., Strong,
K., Roche, S., Sha, M. K., De Mazière, M., Feist, D. G., Iraci, L. T., Roehl, C. M., Retscher, C., and Schepers, D.: Ensemble-based satellite-
600 derived carbon dioxide and methane column-averaged dry-air mole fraction data sets (2003–2018) for carbon and climate applications,
Atmospheric Measurement Techniques, 13, 789–819, <https://doi.org/10.5194/amt-13-789-2020>, publisher: Copernicus GmbH, 2020.
- Schneising, O., Buchwitz, M., Hachmeister, J., Vanselow, S., Reuter, M., Buschmann, M., Bovensmann, H., and Burrows, J. P.: Advances
in retrieving XCH₄ and XCO from Sentinel-5 Precursor: improvements in the scientific TROPOMI/WFMD algorithm, Atmospheric
Measurement Techniques, 16, 669–694, <https://doi.org/10.5194/amt-16-669-2023>, 2023.
- 605 Segers, A., Steinke, T., and Houweling, S.: Description of the CH₄ Inversion Production Chain, [https://atmosphere.copernicus.eu/sites/
default/files/2022-10/CAMS255_2021SC1_D55.5.2.1-2021CH4_202206_production_chain_CH4_v1.pdf](https://atmosphere.copernicus.eu/sites/default/files/2022-10/CAMS255_2021SC1_D55.5.2.1-2021CH4_202206_production_chain_CH4_v1.pdf), 2022.
- Serreze, M. C. and Barry, R. G.: Processes and impacts of Arctic amplification: A research synthesis, Global and Planetary Change, 77,
85–96, <https://doi.org/https://doi.org/10.1016/j.gloplacha.2011.03.004>, 2011.
- Sofieva, V. F., Kalakoski, N., Päivärinta, S.-M., Tamminen, J., Laine, M., and Froidevaux, L.: On sampling uncertainty of satellite ozone
610 profile measurements, Atmospheric Measurement Techniques, 7, 1891–1900, <https://doi.org/10.5194/amt-7-1891-2014>, 2014.
- Stevenson, D. S., Derwent, R. G., Wild, O., and Collins, W. J.: COVID-19 lockdown emission reductions have the potential to ex-
plain over half of the coincident increase in global atmospheric methane, Atmospheric Chemistry and Physics, 22, 14 243–14 252,
<https://doi.org/10.5194/acp-22-14243-2022>, 2022.
- Szopa, S., Naik, V., Adhikary, B., Artaxo, P., Bernsten, T., Collins, W., Fuzzi, S., Gallardo, L., Kiendler-Scharr, A., Klimont, Z., Liao, H.,
615 Unger, N., and Zanis, P.: Short-Lived Climate Forcers, in: Climate Change 2021: The Physical Science Basis. Contribution of Working
Group I to the Sixth Assessment Report of the Intergovernmental Panel on Climate Change, edited by Masson-Delmotte, V., Zhai, P.,
Pirani, A., Connors, S., Péan, C., Berger, S., Caud, N., Chen, Y., Goldfarb, L., Gomis, M., Huang, M., Leitzell, K., Lonnoy, E., Matthews,
J., Maycock, T., Waterfield, T., Yelekçi, O., Yu, R., and Zhou, B., pp. 817–922, Cambridge University Press, Cambridge, United Kingdom
and New York, NY, USA, <https://doi.org/10.1017/9781009157896.008>, type: Book Section, 2021.
- 620 Turner, A. J., Frankenberg, C., and Kort, E. A.: Interpreting contemporary trends in atmospheric methane, Proceedings of the National
Academy of Sciences, 116, 2805–2813, <https://doi.org/10.1073/pnas.1814297116>, 2019.
- Warneck, P.: Chemistry of the Natural Atmosphere, vol. 71 of *INTERNATIONAL GEOPHYSICS SERIES*, Academic Press, 2nd edition edn.,
1999.
- Wendisch, M., Brückner, M., Burrows, J. P., Crewell, S., Dethloff, K., Ebell, K., Lüpkes, C., Macke, A., Notholt, J., Quaas, J., Rinke, A., and
625 Tegen, I.: Understanding Causes and Effects of Rapid Warming in the Arctic, Eos, 98, <https://doi.org/10.1029/2017EO064803>, 2017.

<https://doi.org/10.5194/egusphere-2023-1680>

Preprint. Discussion started: 11 August 2023

© Author(s) 2023. CC BY 4.0 License.



Zhang, Z., Poulter, B., Feldman, A. F., Ying, Q., Ciais, P., Peng, S., and Li, X.: Recent intensification of wetland methane feedback, *Nature Climate Change*, 13, 430–433, <https://doi.org/10.1038/s41558-023-01629-0>, number: 5 Publisher: Nature Publishing Group, 2023.